RSC Advances

ROYAL SOCIETY OF CHEMISTRY

www.rsc.org/advances

Alternating Electric Field Capacitively Coupled Micro-Electroporation

Arie Meir, Boris Rubinsky
6124 Etcheverry Hall,
UC Berkeley, Berkeley,
CA 94720, USA

ABSTRACT

Electroporation of biological solutions is typically performed using galvanically coupled electrodes and the administration of high-voltage, direct current (DC) pulses. Galvanic (DC) coupling enables the flow of Faradaic currents, which produce effects of electrolytic nature. Electrolytic processes can be deleterious to electroporation by causing arcing with high radiative temperature and high-pressure waves, releasing potentially toxic compounds from the electrodes, and introducing by-products of electrolysis into the solution. Our research in micro-electroporation shows that the detrimental effects of electrolysis become more pronounced as the length-scale of the electroporation chamber decreases, i.e. micro-electroporation. A possible solution would be to eliminate galvanic coupling between the electrodes and the electroporation media by coating the electroporation electrodes with a thin layer of dielectric material and using high-frequency AC stimulation for electroporation. In this work, we present a theoretical analysis of a micro-electroporation system in which capacitively coupled electrodes are separated from the electroporated solution by a dielectric. The purpose of this work is to serve as a theoretical basis for further experimental exploration, as well as a design tool for performance optimization. We present a mathematical model supported by *in silico* experimental results.

Index Terms — **Electric Fields, Biophysics, Electric Field Effects.**

1 INTRODUCTION

When a biological cell is exposed to a high electric field, nano-scale defects termed in the literature as pores, occur in its membrane leading to dramatic qualitative changes in the cell's membrane permeability[1, 2]. This biophysical phenomenon has become an important tool in various domains of modern science, medicine and biotechnology [3, 4]. Depending on the strength of the electric field, the cell either reseals the pores and returns to its normal activity, or sustains a sufficient shock that would lead it to death. When the effect is reversible, and the cell can recover from the induced "interference", the electroporation is referred to as reversible [3, 5]. When the damage is too great and the cell is not able to return to its normal function, the phenomenon is naturally called irreversible electroporation [2, 5].

It is widely accepted that electroporation depends on several electric parameters such as electric field strength, polarity, and time of application. With respect to electric field strength, when all the other parameters are kept constant, electroporation is a threshold phenomenon, i.e. an electric field of a magnitude $|\vec{E}| < |\vec{E}_r|$ would not cause electroporation, a field of a magnitude $|\vec{E}_r| < |\vec{E}| < |\vec{E}_i|$ would cause reversible electroporation, and a field of larger magnitude $|\vec{E}| > |\vec{E}_i|$, would lead the cell into irreversible electroporation. In life-science research, reversible electroporation is leveraging the increase in the cell membrane's permeability to introduce molecules, drugs and genes into biological cells[3]. The application of electroporation in the irreversible mode, has recently gained attention in medicine as a potentially useful tissue ablation method[5, 6]. In the food-sterilization field, electroporation was primarily used in the irreversible mode. Pulsed-Electric-Fields (PEF) as the phenomenon is known in this domain, have been studied for several decades as a useful method to kill bacteria and other pathogens naturally proliferating in foods[7].

Most of the research in the field of electroporation, both in life-sciences and food-sterilization domains has been focused on DC electric fields[8]. In such a setting, a typical way to induce electroporation would include bounding the treated medium with a parallel plate configuration of electrodes with DC voltage pulses applied to them. While making the instrumentation simple, the DC-based method of electroporation introduces various electrolytic processes taking place at the electrode-electrolyte boundary[9, 10]. These electrolytic effects include electrochemical reaction with the electrodes and the formation of gases next to the surface of the electrodes.

When exposed to high electric fields, these gases become ionized, which leads to arcing, generation of high local temperatures, and the resulting strong pressure waves. Even in the absence of arcing, the electrolytic processes occurring at the electrolyte-electrode boundary lead to various phenomena, which affect the process of electroporation. These include release of metal ions in the solution and formation of various ionic chemical species that affect cells and electrodes. This problem has not been addressed in the context of biological applications of electroporation, because typically, the protocol involving electroporation is on the order of milliseconds during which the pulses are administered. During this time, the electrolytic effects are not prominent and are normally ignored and not reported. However, there is no doubt that everyone doing experimental work on electroporation must have noticed at least occasional arcing.

Advances in micro-electromechanical technology have made it possible to design a single cell micro-electroporation chip[11]. This has paved the way to the flow-through, single cell, microelectroporation chip[12]. Microelectroporation is an important component in many lab on a chip devices [13]. Attempts to further miniaturize electroporation have led to devices that electroporate only a part of the cell's membrane[14], and to nano-electroporation[15]. Literature survey indicates a growing interest in micro-electroporation, and a thorough review of flow-through micro and nano/electroporation devices can be found in [16]. However, as the size of the effective electroporation volume reduces, geometric considerations begin to play an important role. The effective electroporation volume decreases proportionally to s^3, whereas the active surface area approximately decreases proportionally to s^2; where *s*, is a typical dimension for electroporation. This leads to increased dominance of the mass transport phenomena prompted by electrolysis, since the relative concentrations of the reaction products are higher in smaller scale electroporation chambers. The presence of arcing and electrolytic reactions introduces undesirable effects, which often lead to structural damages of electroporation electrodes as illustrated in Figure 1. We have observed this damage when applying a series of 10 100-microseconds pulses at 5000 V/cm on a sample containing 0.9% NaCl solution. We have used planar interdigital electrodes fabricated using a standard PCB process with 150 um spaces between the anode and the cathode. The applied voltage was 75V. Furthermore, while in micro-electroporation arcing can usually be avoided due to reduced voltages and flow through induced convection, the formation of gas bubbles can lead to interrupted flow in micro-channels, limiting the utility of flow-through electroporation devices[17].

Using AC fields seems like a natural attempt to be taken to address the undesired effects caused by DC electric fields and indeed several recent works report efforts in this direction. In a recent work from our group, bipolar pulses have been used to reduce the effects of electrolysis in a micro-channel, in particular the formation of gas bubbles [17]. However in that work, the electrodes were still galvanically coupled to the electroporated medium, which introduces products of electrolytic reactions into the sample. Also, the authors of the study report, that in order to avoid the electrolytic effects, the bipolar pulse frequency has to be within a limited range. This can be explained by noting that for a slow enough frequency, the square pulses administered still induce short-term electrolysis, which might potentially lead to undesired bubble formation. Another work reported a design of a microfluidic based AC electroporation device[18] using gold-deposited electrodes, which, it was suggested, are less likely to suffer from electrolysis induced electrode erosion. The authors were able to reduce the required AC voltage by fabricating microelectrodes within close proximity to each other (30[um]). However, in our experiments, we find that galvanically coupled gold micro-electrodes are affected by electrolysis (Figure 1).

In this study we propose to address the issue of electrolysis in micro and nano electroporation chips, through elimination of the electrolytic process by capacitively coupling the electroporation electrodes to the medium, across a dielectric layer. To the best of our knowledge there are only two other reported attempts to use capacitively coupled electroporation [19] and [20]; in a context completely different from ours. The approach we propose in this paper is based on a recent work performed in our group which introduced the concept of singularity induced electroporation (SIE)[15]. In the SIE approach, a

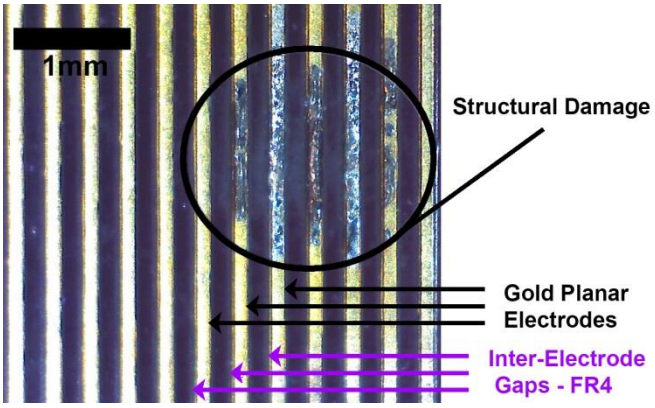

Figure 1 Damaged electrodes used in DC electroporation. Damage was caused by arcing.

specific configuration of planar electrodes eliminates the need in high-voltage electroporators, and can operate from a battery power supply. While our proposed device architecture requires a higher voltage level than currently available from a standard battery, we build upon previous results reported in [15, 21] as we employ a similar geometric configuration of electrodes, but introduce a novel element: a thin dielectric layer which isolates the electrodes from the electrolyte and capacitively couples AC produced electric fields across the layer.

The goal of this study is to advance the concept of AC-based, capacitively coupled, micro and nano-electroporation by developing a set of analytical design tools. Using these tools, we propose to characterize the electroporation process and generate physical insight into the effects of the various design parameters. Our work is mathematical and employs numerical simulations and closed form analytical tools.

In this work, we present a theoretical analysis of a micro-electroporation system in which capacitively coupled electrodes are separated from the electroporated solution by a dielectric. The purpose of this work is to serve as a theoretical basis for further experimental exploration, as well as a design tool for performance optimization. We present a mathematical model supported by *in silico* experimental results, and outline an experimental design which draws intuition and design guidelines from the findings of the *in silico* simulations.

2 METHODS AND MATERIALS

Our mathematical model consists of a 2D cross-sectional geometry with two planar metal electrodes placed on an insulating substrate as depicted schematically in Figure 2 One of the electrodes is grounded and the other one is connected to an AC voltage source.

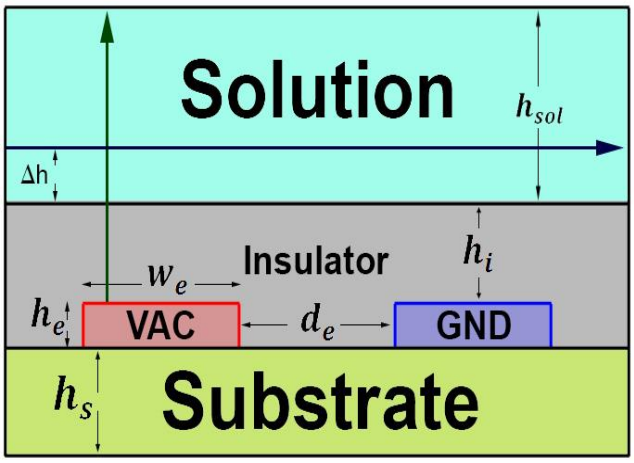

Figure 2 Modeled geometry cross section

The electrodes are coated by a thin layer of insulating material which replaces the galvanic coupling with capacitive link. On top of the insulating material a bulk volume of solution is placed. A simulation of the electroporation process requires solving the field equation. Since our model contains both conductive (electrolyte filled solution) and dielectric materials (insulating coating), both displacement and conduction current exist. The main equation solved is current conservation:

$$\nabla \cdot \vec{J} = 0, \tag{1}$$

Where $\nabla \cdot ()$ is the divergence operator, and $\vec{J}$ stands for the local current density vector. The current density has a conductive component and a displacement component, and it is given by:

$$\vec{J} = \left(\sigma + \varepsilon_0 \varepsilon_r \frac{\partial}{\partial t}\right) \vec{E}. \tag{2}$$

$\vec{E}$ represents the local electric field, σ is the conductivity, ε_0 is the vacuum permittivity and ε_r is the relative permittivity of the material. The electric field is linked to the potential field by the relationship:

$$\vec{E} = -\nabla U. \tag{3}$$

The field equation is solved for the geometrical configuration of Figure 2, subject to Dirichlet boundary condition (sinusoidal voltage), imposed at the electroporation electrodes. The remainder outer surface of the domain was insulated.

Solving the Laplace equation makes it possible to estimate the associated Joule heating P, which is the heat generation rate per unit volume, caused by the electrical field:

$$P = \sigma |\nabla \phi|^2. \tag{4}$$

This term is then added to the Heat equation to represent the amount of heat generated during the electroporation procedure:

$$\nabla \cdot (k \nabla T) + P = \rho C_p \frac{\partial T}{\partial t}. \tag{5}$$

In equation (5), k is the thermal conductivity of the solution, T is the temperature, ρ is the solution density and C_p is the heat capacity of the tissue. The intent of the thermal analysis is to estimate the temperature changes occurring during the electroporation. In a typical application, when electroporation is used for its non-thermal effects, the protocol is often optimized to operate in non-thermal regime[22, 23].

The geometric and electrical parameters characterizing such a configuration are summarized in Table 2. Our analysis is based on a Finite Element Model (FEM) implemented in Comsol Multiphysics 4.3b. Our solution was run on a triangular mesh with boundary layer mesh close to the expected high potential gradient domains. As a means of quality control, the mesh size was reduced to verify that no artifacts are introduced into the solution due to sampling issues. The difference between the solutions was within the relative tolerance specified to the numerical solver (1e-4).

3 RESULTS AND DISCUSSION

3.1 EXPERIMENTAL VALIDATION

The goal of our study is to characterize the concept of AC capacitively coupled micro and nano-electroporation. Numerical simulation and closed form analytical solutions facilitate achieving this goal economically. However, to gain confidence in the mathematical analysis we will first verify the mathematical solution with an experiment. To test the experimental validity of our model, we have

developed a prototype for an insulator coated electrode using Pyralux AC 091200EV (DuPont, USA) flexible circuit material consisting of 12.5 [um] thick Kapton sheet with a 9[um] layer of electro-deposited copper on one side. The 12.5 [um] Kapton layer models the insulation layer we envision in the AC coupled device (Figure 2). The inter-digital electrode was patterned using standard photolithography methods and sealed at the exposed (copper) side by placing an adhesive-based, 200[um] thick, Kapton layer on top of the electrode. The thick insulator layer on the top of the electrodes models the substrate (Figure 2) and its high impedance causes most of the displacement current to flow through the thinner Kapton layer of 12.5[um] . Although our prototypical device uses a larger scale geometry, our motivation behind fabricating it was to confirm the basic assumptions of our model and we demonstrate this confirmation below by comparing the measured impedance with the one predicted by the mathematical model. Figure 3a shows a schematic drawing of an inter-digital electrode, and figure 3b shows a top view of a fabricated electrode. For the experiment, we immersed the insulated electrode into a sodium chloride solution (0.08g/l), designed to have a conductivity of 0.1 [$\frac{S}{m}$] [24].

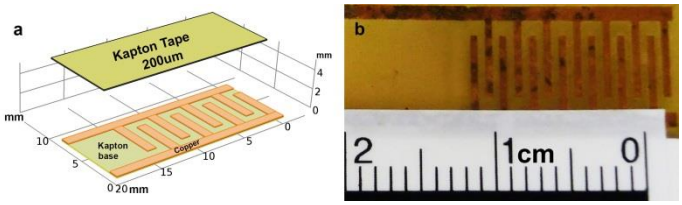

Figure 3 Inter-digital electrodes (a) Schematic, (b) Fabricated Electrode

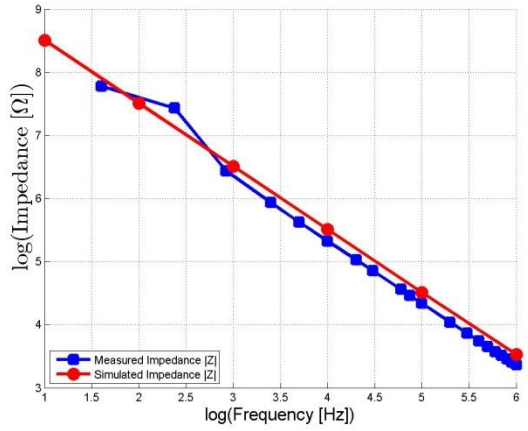

Figure 4 Experimental vs. simulated impedance magnitude data

We then characterized the performance of the electrode using impedance analyzer (Agilent 4294H) measuring the impedance between the two electrodes in the [40Hz-1MHz] frequency range. We have compared the data obtained from a simulated model of equations (1),(2) and (3) with the parameter values of Table 1. To obtain the simulated current through the device, we have used the Electrical Circuit module of Comsol, and added a small current sense resistor in series with the electroporation device depicted in Figure 2. The magnitude of the impedance was obtained from Ohm's law relationship: $|V| = |Z||I|$. The simulated impedance data was compared to the experimentally measured impedance profile, shown in Figure 4. It can be seen that the experimental measurements compare well to the estimates provided by the mathematical model.

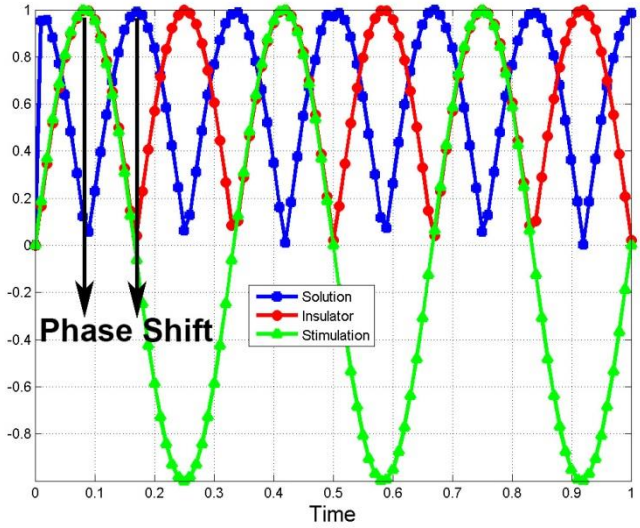

Figure 5 Phase shift in the electrolyte solution

3.2 NUMERICAL EXPERIMENTS

Figures 5-8 were obtained from numerical experiments solving equations (1),(2) and (3) with parameter values from Table 2. The results are presented to provide insight on the effect of a dielectric insulation layer in a capacitively coupled micro-electroporation system.

Figure 5 illustrates the phase shift between the stimulation voltage and the induced voltage in the electrolyte, caused by the dielectric nature of the insulator coating. The presented field magnitudes and the stimulation voltage were normalized for visualization purposes. The electric field in the insulating layer (red curve) is in phase with the stimulating voltage, whereas the electric field in the electrolyte solution (blue curve) is approximately 90 degrees out of phase with the stimulating voltage. The exact phase difference depends on the conductivity on the solution (data not shown).

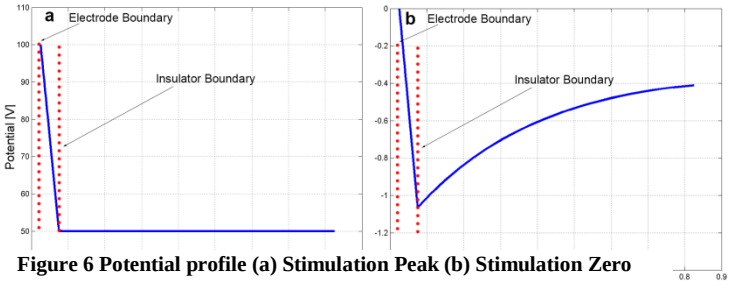

Figure 6 Potential profile (a) Stimulation Peak (b) Stimulation Zero

A representative potential profile along a vertical axis (shown green in Figure 2) is presented in Figure 6. Figure 6a shows the potential profile when the stimulation voltage is at its peak: The entire voltage drops on the insulator, and there is no potential drop (i.e. no field) inside the electrolyte solution. Figure 6b shows the potential profile when the stimulation voltage is at its zero: at this point a voltage drop inside the electrolyte is induced by the lagging-behind displacement current.

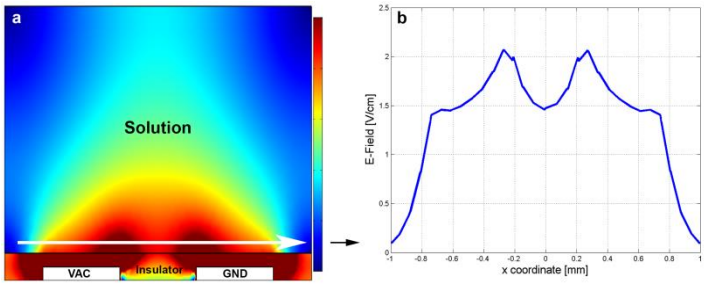

Figure 7 E-Field in a representative configuration (a) Field Magnitude Map (b) Typical Field Profile

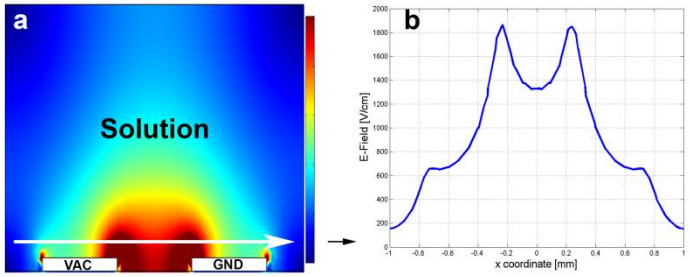

Figure 8 E-Field without insulating barrier. (a) Field Magnitude Map (b) Typical Field Profile

Figure 7a shows a map of the peak field magnitude of a representative configuration. Figure 7b shows a field profile taken inside the electroporated solution adjacent to the insulating surface. The measured slice is shown as a blue, horizontal arrow on Figure 2. A vertical step Δh equal to 10% of the insulator thickness h_i was used as the height above the insulating surface for measuring the profile.

For comparison, we have simulated a configuration without the insulating layer. Figure 8a shows a map of the peak field magnitude of a comparable configuration. Figure 8b shows a field profile taken inside the electroporated solution at the same location relative to the electrodes as in figure 5. Figure 8 indicates that while there is little qualitative difference between the two configurations, the quantitative difference is large: the field is 2-3 orders of magnitude higher without the insulator. This is clearly a drawback of the capacitative coupling mode, as a much higher external voltage is required in order to provide the same electric field in the medium.

Having said that, we present a sensitivity study in a later section, which provides an insight on the effect of different system parameters as well as concrete design guidelines for mitigating the effect.

3.3 LUMPED-ELEMENT MODEL

The design of AC capacitively coupled micro and nano-electroporation systems may benefit from a simplified, lumped-element circuit model that can be used to get a first order approximation of the effects of various electric parameters. Such a design is presented in Figure 9. The insulating layers were modeled as two capacitors C_1 and C_2, while the electrolyte was modeled as a linear

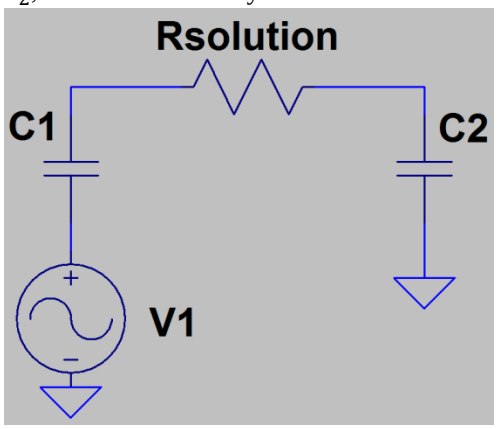

Figure 9 Lumped Element Model

resistor $R_{solution}$. Parallel plate capacitor model was used to estimate the capacitance. Conductance was then estimated using the systems geometry and the electric properties of the materials:

$$C = \frac{\epsilon_r \cdot \epsilon_0 \cdot A_c}{d}, G = \frac{\sigma \cdot A_{G_G}}{l}. \quad (6)$$

In equation (6), C stands for capacitance, ϵ_r is the relative permittivity of the material. ϵ_0 is the dielectric permittivity of free space, A_c is the plate area and d is the distance between the plates. G is the conductance, σ represents the material conductivity, A_G represents the cross-sectional area of the conductor and l represents the length of the conductor. Since the geometry of our model does not map directly into the formulations of equation (6),

we have used these estimates: $A_c = \boldsymbol{w_e} \times 1, d = \boldsymbol{h_i}$, $\mathrm{A_G} = \boldsymbol{w_e} \times 1, l = \boldsymbol{2d_e}$. See Table 2 for numerical values specification. Using the nominal configuration, the capacitance and the conductance are estimated and the current through the system is estimated using Ohm's law, and taking into account the electrical impedance of the equivalent circuit:

$$\boldsymbol{I} = \frac{\boldsymbol{V}}{\boldsymbol{SF}\,(\,\boldsymbol{Z_{equivalent}})} = \frac{\boldsymbol{V}}{\frac{\boldsymbol{SF}}{\boldsymbol{wC_1}} + \boldsymbol{SF}\cdot\,\boldsymbol{R_{solution}} + \frac{\boldsymbol{SF}}{\boldsymbol{wC_2}}}\,. \qquad (7)$$

A typical approach allowing accounting for a complex geometry in terms of a more simplified geometry, uses a shape factor (SF) that correlates between the two configurations. The SF is calculated from the exact solution, by comparing the actual current calculated in a certain complex geometrical configuration with calculations in expression 7, and evaluating the SF yielding identity of both sides. Because the equations are linear the SF value remains constant when linear scaling of dimensions are used and does not change much in the neighborhood of the estimated geometry. In our case the SF used was 193.53. Figure 10 shows the relative impedance of the capacitative layer vs. the resistive impedance of the electrolyte solution.

The geometric and electrical parameters were set to their nominal values listed in Table 2, and only the insulator thickness was varied. It can be seen from this figure that for the taken parametric configuration an insulating layer thicker than 100nm causes most of the voltage drop to occur across the capacitative link.

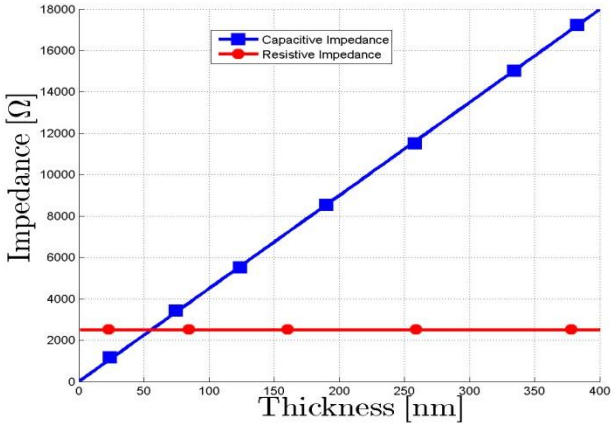

Figure 10 Relative Impedance Magnitude

3.4 DESIGN CONSIDERATIONS

Following are studies dealing with various design consideration of importance in an AC capacitively coupled micro and nano-electroporation system.

1) *Dielectric breakdown considerations*

One of the key design constraints of the capacitively coupled electrodes is the dielectric breakdown threshold of the insulating layer. Dielectric films tend to exhibit greater dielectric strength than thicker samples of the same material. For instance, the dielectric strength of silicon dioxide films of a few hundred [nm] to a few [um] thick is approximately $0.5\,\frac{GV}{m}$ [25]. The dielectric breakdown voltage determines the frequency of the stimulation and the range of insulator thickness values which can be used under idealized conditions. In reality, materials exhibit defects which lower their breakdown voltage[25], and the exact values will have to be determined experimentally. In this work we take the dielectric breakdown into consideration during the parametric sensitivity analysis in a later section**.**

2) *Dosage Considerations*

Multiple models for optimizing electroporation protocols were reported [22, 23, 26], but for the most part they deal with DC pulses and do not address AC high-frequency stimulation. Considering electroporation as a threshold phenomenon, the following model could be used to estimate the time that the sample is exposed to the supra-threshold e-field magnitude. In the equation outlined below $t_{exposure}$ represents the time that the sample is exposed to supra-threshold e-field, f represents the stimulation frequency, E_{peak} is the peak magnitude of the electric field and $E_{threshold}$ is the ratio of the peak e-field magnitude that leads to electroporation. N_{cycles} stands for the number of stimulation cycles. The detailed derivation of equation (8) is presented in the appendix.

$$t_{exposure}\left(f, E_{peak}, E_{threshold}\right) = \qquad (8)$$
$$4\cdot\frac{1}{f}\cdot N_{cycles}\cdot\left[\frac{\frac{\pi}{2}-\arcsin\left(\frac{E_{threshold}}{E_{peak}}\right)}{2\pi}\right].$$

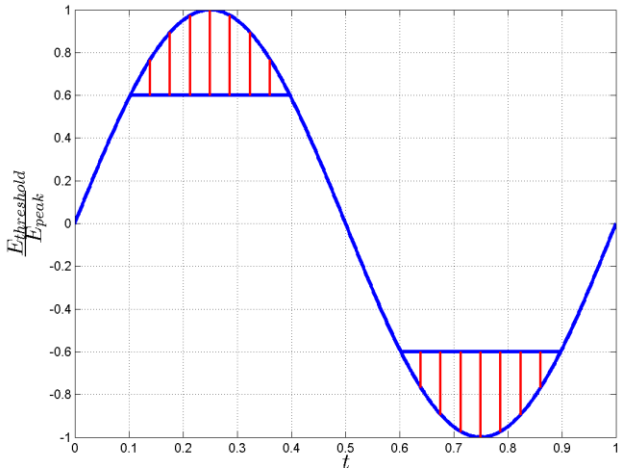

Figure 11 Supra-Threshold E-Field Regions

Figure 11 shows a single period of a sinusoidal E-Field with supra-threshold regions marked for a threshold of 0.6. A typical electroporation protocol[27] uses a sequence of 10 pulses of 100[us] with 1 second interval between adjacent pulses. We have used the proposed mathematical model to develop a comparable AC stimulation protocol. First, the peak e-field was estimated in the sample of interest using the transient solution of the field equation. Since we assume capacitive coupling, the peak e-field magnitude depends on the geometry of the problem and the frequency of stimulation. Once a threshold field magnitude is determined depending on the stimulation protocol[28], the required number of stimulation periods can be found.

3) *Thermal Analysis*

One of the prominent features of classical electroporation, and the reason for its growing popularity in life science research and medicine, is the relative insignificance of thermal effects. In a typical setting, the DC pulses normally used have to be short enough and far apart from each other to avoid causing a significant change in the temperature of the electroporated medium. Joule-heating induced thermal effects in capacitively coupled electroporation were estimated by solving the heat equation in the entire domain. To reduce computational cost, the overall current was estimated without solving the heat

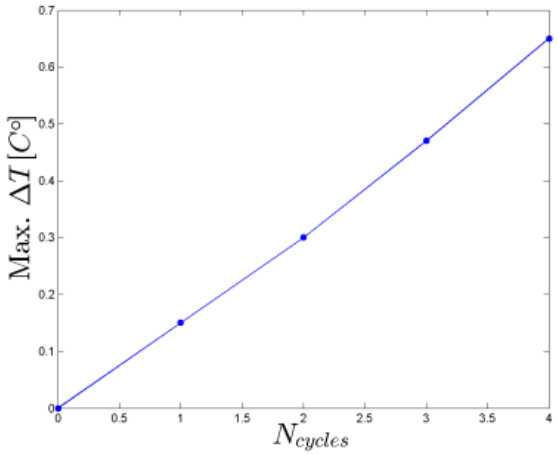

Figure 12 Maximum Temperature

equation and then it was prescribed as a transient boundary condition to a simplified problem which didn't include the insulating layer. The mesh without the insulating layer was significantly simpler (1650 elements compared to 219508 elements with a 250nm thick insulating layer), yet physically equivalent in terms of the heat generated in the electrolyte. Depending on the thickness of the insulator and the stimulation frequency, the impedance of the capacitative interface changes relative to the resistive electrolyte. This affects the relative voltage drop inside the bulk of the electrolyte solution, affecting the field and therefore the Joule heating of the solution. A conservative estimate (assuming all the voltage dropping inside the bulk solution) is presented in figure 12. Figure 12 was obtained from the solution of equations (1)-(5) with the nominal parameter values from Table 2, which simulate the Joule heating of the solution. Under this configuration, a rate of temperature raise is approximately $0.15C^{\circ}/Cycle$. This estimate of the thermal effect of electroporation can be incorporated into protocol design.

4) *Field Decay Profile*

Field penetration depth is an important design metric for practical applications of electroporation to bulk biological solutions. Simulation results indicate that the field strength decays exponentially with the distance from surface of the dielectric coating. The main parameter affecting the decay rate is the solution conductivity which determines the current density and therefore the field in the solution. Figure 13 was obtained from the solution of equations (1)-(3) with parameter values taken from Table 2. Figure 13 shows characteristic decay profiles for several representative conductivities: $0.01[\frac{S}{m}]$ and $0.001[\frac{S}{m}]$. The field strength and the distance from the reference point were normalized for easier visualization. As expected, the more conductive is the solution, the faster is the decay of the e-field.

5) *Sensitivity Analysis*

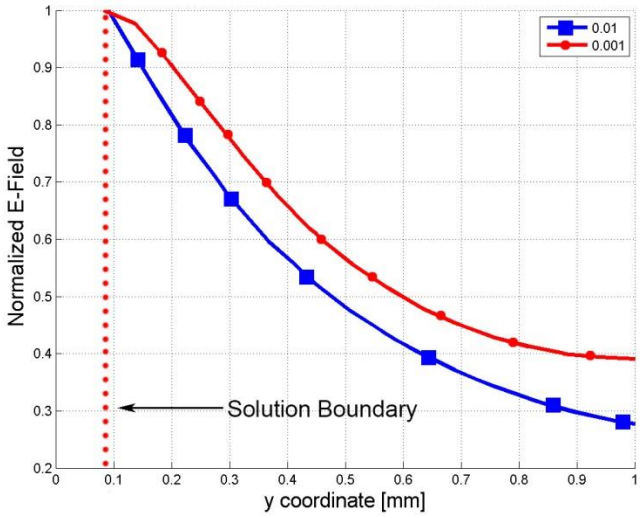

Figure 13 Field Decay Profile. Representative conductivities[$\frac{S}{m}$] shown.

When studying electroporation, the electric field magnitude in the sample is one of the key parameters that characterize the nature of the effect. To test the effect of different electric and geometric parameters on the field strength, we have conducted several parametric studies. Figures 14a-14e present the variation in peak magnitude of electric field as a function of different system parameters swept over a typical experimental range. The nominal parameter values used for these simulations are summarized in Table 2. The equations (1)-(3) were solved while having all the parameters fixed at the values given by Table 2, besides the parameter for which the sensitivity is being analyzed.

Figure 14a presents the sensitivity of the peak electric field magnitude to the thickness of the insulating layer. The green horizontal line indicates the breakdown threshold field for the insulator, taken from[25]. All the simulation parameters were taken from Table 2 besides the stimulation voltage. For this simulation, the applied voltage was chosen $V_{stim} = 500V$ (Amplitude) in order to demonstrate the effect of the breakdown voltage threshold. The insulator thickness varied between 250[nm] and 50[um]. The red straight line in a log-log plot indicates exponential dependence of the peak electric-field magnitude on the thickness of the insulating layer. The overlaying red lines with different markers indicate small sensitivity of the peak insulator e-field on the stimulation frequency. This can be explained by noting the phase shift between the e-field inside the solution and the insulator. When the field inside the insulator is at its peak, the voltage drop inside the solution is almost zero due to the lagging, therefore the stimulation frequency has almost no effect. Figure 14a shows that a prescribed stimulation voltage, determines a minimum thickness of the insulator. For the simulation parameters used, the minimal insulator thickness was found to be 500[nm].

The blue lines in Figure 14a show the sensitivity of the peak e-field inside the solution to variation in frequency and insulator thickness. It can be observed that higher frequency leads to a higher peak field in the solution as predicted from the simple lumped-element model. The peak field values were measured at a distance of Δh above the insulator: Δh was chosen as 10% of the insulator thickness h_i. Simulation data presented in Figure 14a indicates that increasing the frequency of the stimulation would increase the peak e-field strength in the solution. While our simulation accounts for the large scale physical phenomena occurring in the electroporation chamber, biological aspects related to the electrical properties of the cell's membrane are not accounted for.

Figure 14b shows the dependence of peak e-field in the electroporated solution on the stimulation frequency. To generate this figure, equations (1)-(3) were solved using parameter values listed in Table 2, while varying the frequency in the 10[Hz]-10[MHz] range. A straight line in log-log plot indicates an exponential dependence which is consistent with the lumped circuit model, i.e. equation (7).

While the absolute thickness of the insulator determines the electric field magnitude, the lateral dimensions such as the electrode width and the inter-electrode gap, vary only relatively to the thickness of the insulator. The sensitivity of the peak e-field inside the electroporation medium to the ratio of inter-electrode gap and insulator thickness is presented in Figure 14c. To generate this figure, equations (1)-(3) were solved using parameter values listed in Table 2, while varying the ratio of inter-electrode gap to insulator thickness in the 1-10 range. The simulation data suggests that minimizing the gap between the electrodes would lead to increased e-field in the solution. This could be used as a design guideline, i.e. having multiple thin planar electrodes separated by a thin gap.

Figure 14d shows the dependence of peak e-field in the electroporation medium on the dielectric constant of the insulating material. To generate this figure, equations (1)-(3) were solved using parameter values listed in Table 2, while varying the dielectric constant of the insulator in the range 2-6. The simulation data indicates that an insulator with a higher dielectric constant would lead to a higher effective e-field. This finding is consistent with the lumped-element model prediction, since the dielectric constant of the insulator increases the capacitance, which in turn leads to a high voltage drop on the resistive solution. It also provides a guideline in the choice of insulating material: while we typically used SiO_2 as our nominal insulator with a dielectric constant of 3.9, other insulating materials have dielectric constants 1-2 orders of magnitude higher, e.g. $TiO_2$with a constant in the range of 86-173[29].

Figure 14e shows the dependence of peak e-field in both the electroporation medium and the insulating layer on the conductivity of the electroporation medium. To generate this figure, equations (1)-(3) were solved using parameter values listed in Table 2, while varying the solution conductivity in the range of $[0.001\frac{S}{m}, 1\frac{S}{m}]$. The red line, corresponding to the peak e-field magnitude inside the insulator is almost flat for the entire range of conductivities tested. The small decline in the peak e-field inside the insulator corresponds to a more "even" distribution of the voltage drop between the chamber components, when the electroporated medium becomes less conductive, i.e. more polarizable. The straight blue line corresponding to the peak e-field inside the solution corresponds to an exponential dependence. This indicates that generating a high electric field inside a highly conductive medium is a challenge. This behavior is familiar to researchers experimenting with electroporation of strong ionic solutions, and is sometimes addressed by removing ionic contents from the electroporation medium for better results.

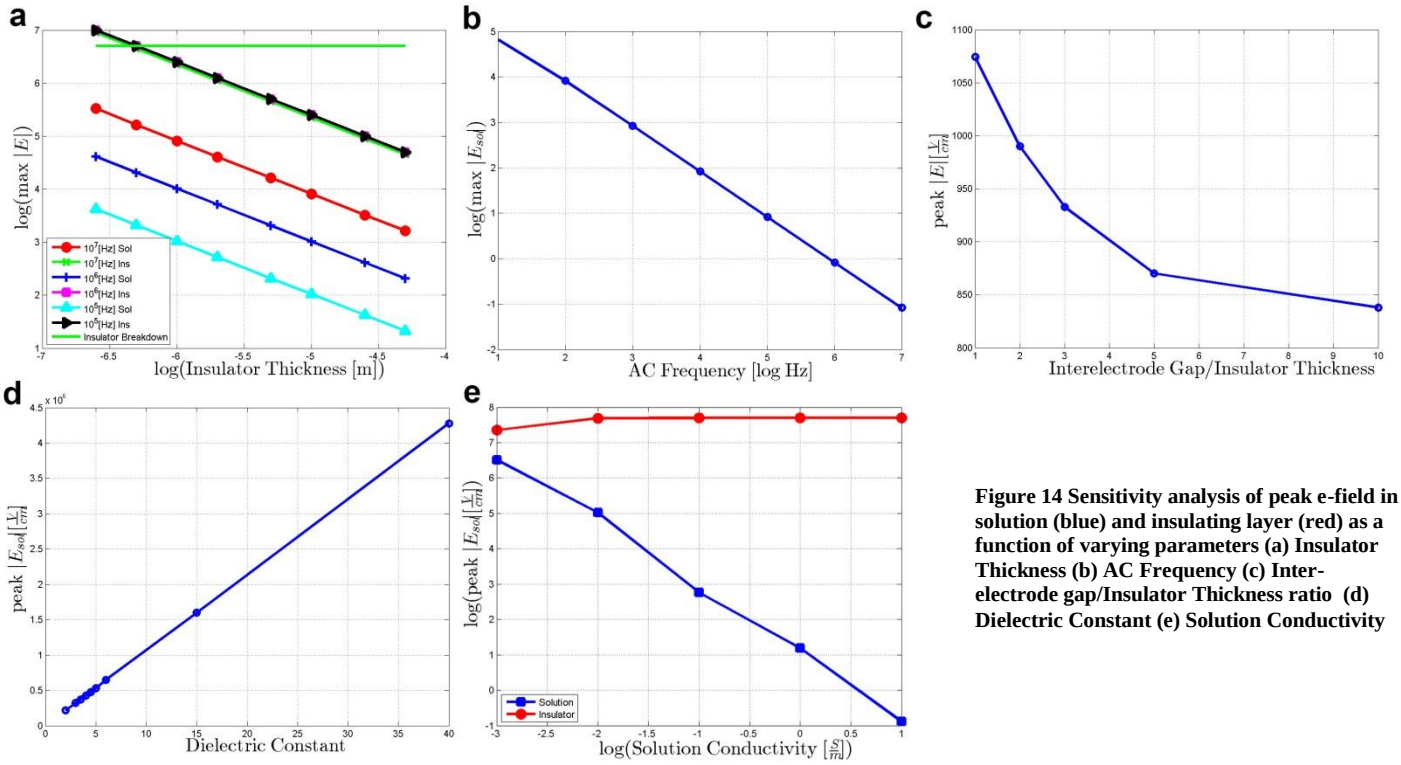

Figure 14 Sensitivity analysis of peak e-field in solution (blue) and insulating layer (red) as a function of varying parameters (a) Insulator Thickness (b) AC Frequency (c) Inter-electrode gap/Insulator Thickness ratio (d) Dielectric Constant (e) Solution Conductivity

3.5 DESIGN EXAMPLES AND LIMITATIONS

In this section we illustrate a typical design process for an AC coupled micro-electroporation system. Assuming that our target parameters are a threshold e-field of 300 $[\frac{V}{cm}]$ commonly reported for reversible electroporation, a solution with conductivity of 0.1 $[\frac{S}{m}]$, and a typical protocol of 8 pulses, each pulse lasting 100 microseconds. Given these input parameters, and assuming our fabrication process uses $SiO_2$for coating, we can employ the model in order to determine the required insulator thickness, the stimulation frequency and amplitude, and the number of AC cycles. Using a frequency of $100kHz$, we fall within the classical sub-MHz region and also reduce the need in a specialized high frequency power supply. Our simulation results, using equations (1)-(3), using the design parameters in Table 2, show that using a 100V (peak) stimulation on an electrode separated from the solution by a 500[nm] layer of SiO_2, would result in a peak e-field magnitude of 320 $[\frac{V}{cm}]$ penetrating several micrometers deep into the solution before dropping to sub-threshold level. Using 0.75 as the $\frac{E_{effective}}{E_{peak}}$ ratio, the number of cycles yielding a comparable AC stimulation protocol is 22, which leads to peak increase in temperature of at most $3.3C^{\circ}$per single stimulation AC burst. While these parameters will require experimental validation and adjustment for unaccounted factors such as material non-idealities, convective cooling, fabrication non-idealities, we see our contribution in a theoretically based analytic tools that can help focus and troubleshoot future experimental efforts.

We see the main limitation of micro/nano-electroporation in general and our work in particular in the relatively low ratio of active/total volume which we define as the fraction of the volume where super-threshold magnitude of electric field is achieved. The precise numeric value of this ratio depends on the threshold the field and the overall size of the device, but it is by all means much less than traditional electroporation devices. We humbly acknowledge that this work is a first of its kind and it was developed as a first step towards exploring electroporation through AC fields. We set as a goal to test the basic feasibility using numerical tools before additional efforts are allocated to experimental efforts. We envision ameliorating the active volume limitation by addressing the problem in two directions: first, the geometry of the device itself – by stacking a series of thin devices close to each other we could further increase the active volume to non-active volume ratio in the aggregated device. An alternative geometry might include a flow-through architecture where the liquid to be sterilized is passed through a single focus point where electroporation occurs. While this might not increase the active volume, this approach would lead to a more reliable sterilization process – by definition all liquid will have to pass through the "active region". The second direction to work around the limitations, would involve mixing: we envision a mechanical mixing system which circulates the liquid in the sterilization chamber which increases the probability that any micro-organism present in the solution would be sooner or later exposed to the super-threshold electric field. The focus of this work was on the feasibility of generating electroporation level fields without galvanic coupling and no performance optimization

attempts were made. We intend to address design optimization in future work.

4 CONCLUSION

The goal of our study was to lay ground for experimental exploration of capacitively coupled AC electroporation. We accomplished our goal by developing a set of analytic and numerical tools, which provide physical insight about the importance of different parameters, and equip us with practical design guidelines. Due to the large parametric space available for exploration, we find simulation tools especially useful for focusing experimental efforts.

Based on the simulation results, we have found that due to the dielectric nature of the insulating layer, the displacement current dominates, hence it is 90 degrees out-of-phase with the stimulation voltage. In the electrolyte solution however, the conduction current dominates over the displacement current. Since it is the conduction current that induces the potential over the electrolyte, it should be expected that the voltage in the electrolyte will be out-of-phase with the applied stimulation voltage.

Sensitivity analysis reveals that the key parameters affecting the peak magnitude of the e-field include the thickness of the insulating dielectric coating the electrodes, and the frequency of the administered AC stimulation. This result confirms the intuition provided by the crude, lumped-circuit model, where a thinner dielectric corresponds to a larger capacitance. Larger capacitance, coupled with higher stimulation frequency, leads to increased voltage drop on the electrolyte solution, yielding higher e-field. Similar argument can explain the increase in peak electric field as the dielectric constant of the insulator increases. While increasing the stimulation frequency increases the e-field in the electroporation sample, when going beyond the 1MHz range, one might need to consider cell membrane effects. For a typical cell, the specific membrane capacitance is such that starting at 1MHz, the membrane increasingly behaves as a short-circuiting element. This affects the way that the voltage is distributed on the different components of a single cell. This combination of constraints, guides us to focus the experimental range of frequencies for exploration in the hundreds of kHz range.

In addition to revealing key parameters, the results of our numerical experiments indicate that the peak values of the electric field occur next to the edges of the electrodes. This suggests that having multiple, laterally narrow electrodes might be preferable in terms of optimizing the supra-threshold region.

A thermal analysis taking into account the Joule effects produced by the electric field indicates that the temperature changes in the case of capacitive coupling are relatively low for a typical configuration. For other geometries and/or electric parameters, the thermal analysis provides a modeling tool, which can be used to design and optimize electroporation protocols.

In summary, our *in silico* simulations suggest that capacitively coupled electrodes might be a feasible approach for *in vitro* electroporation of biological solutions. AC insulated electroporation might eliminate the effects of electrolysis, which reduce experimental efficiency and impede technological advances. In our future work we intend to expand the experimental effort and perform electroporation experiments using AC coupled electrodes.

APPENDIX

Table 1 Model electric parameters used for experimental validation

h_e	Electrode Thickness	9[um]
w_e	Electrode Width	1000[um]
h_i	Insulator Coating Thickness	12.5[um]
d_e	Inter-electrode Gap Distance	1000[um]
ε_i	Insulator Dielectric Constant	3.9, Kapton from [30]
ε_s	Solution Dielectric Constant	79.5 from [31]
σ_i	Insulator Conductivity	0.5e-14 from [30]
σ_s	Solution Conductivity	0.1[S/m]
V_{stim}	Stimulation Voltage	100[V]
h_s	Substrate Thickness	200[um]
h_{sol}	Solution Height	2000[um]

Table 2 Model electric and thermal parameters used for numerical experiments

h_e	Electrode Thickness	50[um]
w_e	Electrode Width	500[um]
h_i	Insulator Coating Thickness	250[nm]
d_e	Inter-electrode Gap Distance	500[um]
ε_i	Insulator Dielectric Constant	3.9, SiO_2 from [32]
ε_s	Solution Dielectric Constant	79.5 from [31]
σ_i	Insulator Conductivity	1e-14 from [32]
σ_s	Solution Conductivity	0.1[S/m]
V_{stim}	Stimulation Voltage	100[V]
f_{stim}	Stimulation Frequency	10^5 [Hz]
C_p	Specific Heat Capacity	4.186 $[J/g\,°C]$ from[33]
k	Thermal Conductivity	0.58 $[W\,m^{-1}\,K^{-1}]$ from[34]
V_{bd}	Breakdown Voltage	5[MV/cm] from[25]

h_s	Substrate Thickness	500[um]
h_{sol}	Solution Height	1000[um]

SUPRA-THRESHOLD E-FIELD REGION

A possible model for estimating the time that the sample is exposed to the supra-threshold e-field magnitude is presented below.

If we define $t_{exposure}$ represents the time that the sample is exposed to supra-threshold e-field, f represents the AC stimulation frequency, E_{peak} is the peak magnitude of the electric field and $E_{threshold}$ is the ratio of the peak e-field magnitude that leads to electroporation. To clarify, if E_{peak} is 300V/cm and we assume that electroporation occurs at 240V/cm, then $E_{threshold}$ would be chosen as 240/300 = 0.8. N_{cycles} stands for the number of stimulation cycles.

Focusing on a single quarter of a cycle of the AC sinusoid, $\arcsin\left(\frac{E_{threshold}}{E_{peak}}\right)$ gives us the angle in radians which corresponds to a sub-threshold field. By subtracting this angle from $\frac{\pi}{2}$, we get the complimentary angle, corresponding to supra-threshold field. Dividing by the length of the cycle in radians and multiplying by 4 (to compensate for initially taking only a quarter) we get the relative proportion of the cycle in which the field is above the specified threshold. By factoring in the period given by $T_{period} = \frac{1}{f}$ and scaling by the number of cycles, we get the total time that the sample has been exposed to a supra-threshold electric field. To summarize:

$$t_{exposure}(f, E_{peak}, E_{threshold}) = 4 \cdot \frac{1}{f} \cdot N_{cycles} \cdot \left[\frac{\frac{\pi}{2} - \arcsin\left(\frac{E_{threshold}}{E_{peak}}\right)}{2\pi}\right].$$

REFERENCES

[1] J. C. Weaver, "Electroporation: a dramatic, nonthermal electric field phenomenon," in *Proceedings of the first world congress for electricity and magnetism in biology and medicine. Lake Buena Vista, Florida: Academic Press* vol. 14, ed, 1992.

[2] J. C. Weaver and Y. A. Chizmadzhev, "Theory of electroporation: a review," *Bioelectrochemistry and Bioenergetics,* vol. 41, pp. 135-160, 1996.

[3] E. Neumann, A. E. Sowers, and C. A. Jordan, *Electroporation and electrofusion in cell biology*: Plenum Publishing Corporation, 1989.

[4] S. Haberl, D. Miklavcic, G. Sersa, W. Frey, and B. Rubinsky, "Cell membrane electroporation-Part 2: the applications," *Electrical Insulation Magazine, IEEE,* vol. 29, pp. 29-37, 2013.

[5] R. Davalos, L. Mir, and B. Rubinsky, "Tissue ablation with irreversible electroporation," *Annals of biomedical engineering,* vol. 33, pp. 223-231, 2005.

[6] B. Rubinsky, "Irreversible electroporation: implications for prostate ablation," *Technology in cancer research & treatment,* vol. 6, 2007.

[7] H. L. Lelieveld, S. Notermans, and S. De Haan, *Food preservation by pulsed electric fields: from research to application*: Woodhead, 2007.

[8] M. Behrend, A. Kuthi, X. Gu, P. T. Vernier, L. Marcu, C. M. Craft, *et al.*, "Pulse generators for pulsed electric field exposure of biological cells and tissues," *Dielectrics and Electrical Insulation, IEEE Transactions on,* vol. 10, pp. 820-825, 2003.

[9] P. Turjanski, N. Olaiz, P. Abou-Adal, C. Suarez, M. Risk, and G. Marshall, "pH front tracking in the electrochemical treatment (EChT) of tumors: Experiments and simulations," *Electrochimica Acta,* vol. 54, pp. 6199-6206, 2009.

[10] P. Turjanski, N. Olaiz, F. Maglietti, S. Michinski, C. Suarez, F. V. Molina, *et al.*, "The role of pH fronts in reversible electroporation," *PloS one,* vol. 6, p. e17303, 2011.

[11] Y. Huang and B. Rubinsky, "Micro-electroporation: improving the efficiency and understanding of electrical permeabilization of cells," *Biomedical Microdevices,* vol. 2, pp. 145-150, 1999.

[12] Y. Huang and B. Rubinsky, "Micro-electroporation: improving the efficiency and understanding of electrical permeabilization of cells," *Biomedical Microdevices|Biomedical Microdevices,* vol. 2, pp. 145-50, 1999.

[13] H. Andersson and A. van den Berg, Eds., *Lab on Chips for Cellomics.* P.O. Box 17, 3300 AA Dordrecht, The Netherlands.: Springer, 2004, p.^pp. Pages.

[14] R. E. Díaz-Rivera and B. Rubinsky, "Electrical and thermal characterization of nanochannels between a cell and a silicon based micro-pore," *Biomedical Microdevices,* vol. 8, pp. 25-34, 2006.

[15] G. D. Troszak and B. Rubinsky, "Self-powered electroporation using a singularity-induced nano-electroporation configuration," *Biochemical and Biophysical Research Communications,* vol. 414, pp. 419-424, 2011.

[16] T. S. Santra and F. G. Tseng, "Recent Trends on Micro/nanofluidic Single Cell electroporation," *Micromachines,* vol. 4, pp. 333-356, 6 September 2013 2013.

[17] R. Ziv, Y. Steinhardt, G. Pelled, D. Gazit, and B. Rubinsky, "Micro-electroporation of mesenchymal stem cells with alternating electrical current pulses," *Biomedical microdevices,* vol. 11, pp. 95-101, 2009.

[18] H. Lu, M. A. Schmidt, and K. F. Jensen, "A microfluidic electroporation device for cell lysis," *Lab on a Chip,* vol. 5, pp. 23-29, 2005.

[19] D. M. French, M. D. Uhler, R. M. Gilgenbach, and Y. Lau, "Conductive versus capacitive coupling for cell electroporation with nanosecond pulses," *Journal of Applied Physics,* vol. 106, pp. 074701-074701-4, 2009.

[20] B. Roodenburg, "Pulsed Electric Field treatement of packaged food.," PhD PhD, Technical University Delft, Netherlands, 2011.

[21] G. D. Troszak and B. Rubinsky, "A theoretical analysis of the feasibility of a singularity-induced micro-electroporation system," *PloS one,* vol. 6, p. e18523, 2011.

[22] R. V. Davalos, B. Rubinsky, and L. M. Mir, "Theoretical analysis of the thermal effects during in vivo tissue electroporation," *Bioelectrochemistry,* vol. 61, pp. 99-107, 2003.

[23] R. V. Davalos and B. Rubinsky, "Temperature considerations during irreversible electroporation," *International journal of heat and mass transfer,* vol. 51, pp. 5617-5622, 2008.

[24] P. C. Ho, D. A. Palmer, and R. E. Mesmer, "Electrical conductivity measurements of aqueous sodium chloride solutions to 600 C and 300 MPa," *Journal of solution chemistry,* vol. 23, pp. 997-1018, 1994.

[25] H. Bartzsch, D. Glöß, P. Frach, M. Gittner, E. Schultheiß, W. Brode, *et al.*, "Electrical insulation properties of sputter-deposited SiO2, Si3N4 and Al2O3 films at room temperature and 400° C," *physica status solidi (a),* vol. 206, pp. 514-519, 2009.

[26] P. A. Garcia, J. H. Rossmeisl, R. E. Neal, T. L. Ellis, and R. V. Davalos, "A parametric study delineating irreversible electroporation from thermal damage based on a minimally invasive intracranial procedure," *Biomedical engineering online*, vol. 10, p. 34, 2011.

[27] J. A. Nickoloff, *Animal cell electroporation and electrofusion protocols* vol. 48: Springer, 1995.

[28] H. Y. Wang and C. Lu, "Microfluidic electroporation for delivery of small molecules and genes into cells using a common DC power supply," *Biotechnology and bioengineering*, vol. 100, pp. 579-586, 2008.

[29] U. Diebold, "The surface science of titanium dioxide," *Surface science reports*, vol. 48, pp. 53-229, 2003.

[30] "Kapton Polyimide Film : Technical data sheet," *http://www2.dupont.com/Kapton/en_US/assets/downloads/pdf/CR_H-54506-1.pdf*.

[31] C. Wohlfarth, "Dielectric constant of water," in *Supplement to IV/6*, ed: Springer, 2008, pp. 29-42.

[32] T. Gupta, *Copper interconnect technology*: Springer, 2009.

[33] N. B. Vargaftik, "Handbook of physical properties of liquids and gases-pure substances and mixtures," 1975.

[34] N. Fofonoff, "Physical properties of seawater: A new salinity scale and equation of state for seawater," *Journal of Geophysical Research: Oceans (1978–2012)*, vol. 90, pp. 3332-3342, 1985.

Arie Meir is a PhD student in the Biophysics program of UC Berkeley. He received the B.Sc. degree from the Technion, Israel Institute of Technology, Haifa, Israel in 2003, the M.Sc. degree from the Hebrew University of Jerusalem in 2009. In addition to interest in modeling biophysical systems, Arie is interested in medical imaging and device design.

Boris Rubinsky received the Ph.D. degree from the Massachusetts Institute of Technology, Cambridge, in 1980. His thesis research was in the area of bioengineering. Since 1980, he is a Professor at the University of California, Berkeley. During his career, he has developed several areas of research in bioengineering, including pioneering the field of imaging monitored minimally invasive surgery in general and cryosurgery in particular. He worked on imaging technologies with ultrasound, MRI, optical imaging, and electrical imaging. He performed studies on cold tolerant and freezing tolerant animals and developed microelectromechanical bionic technology for real time interaction between electromagnetic fields and individual cells. He has published over 200 research articles and has more than 20 issued patents.